PCCP

PAPER

View Article Online
View Journal | View Issue

Cite this: *Phys. Chem. Chem. Phys.*, 2021, **23**, 1114

Mechanistic insights into carbon dioxide utilization by superoxide ion generated electrochemically in ionic liquid electrolyte†

Ahmed Halilu, [ab] Maan Hayyan, *[bc] Mohamed Kheireddine Aroua, *[de] Rozita Yusoff *[a] and Hanee F. Hizaddin [ab]

Understanding the reaction mechanism that controls the one-electron electrochemical reduction of oxygen is essential for sustainable use of the superoxide ion ($O_2^{\bullet-}$) during CO_2 conversion. Here, stable generation of $O_2^{\bullet-}$ in butyltrimethylammonium bis(trifluoromethylsulfonyl)imide [BMAmm$^+$][TFSI$^-$] ionic liquid (IL) was first detected at −0.823 V *vs.* Ag/AgCl using cyclic voltammetry (CV). The charge transfer coefficient associated with the process was ∼0.503. It was determined that [BMAmm$^+$][TFSI$^-$] is a task-specific IL with a large negative isovalue surface density accrued from the [BMAmm$^+$] cation with negatively charged C(sp^2) and C(sp^3). Consequently, [BMAmm$^+$][TFSI$^-$] is less susceptible to the nucleophilic effect of $O_2^{\bullet-}$ because only 8.4% $O_2^{\bullet-}$ decay was recorded from 3 h long-term stability analysis. The CV analysis also detected that $O_2^{\bullet-}$ mediated CO_2 conversion in [BMAmm$^+$][TFSI$^-$] at −0.806 V *vs.* Ag/AgCl as seen by the disappearance of the oxidative faradaic current of $O_2^{\bullet-}$. Electrochemical impedance spectroscopy (EIS) detected the mechanism of $O_2^{\bullet-}$ generation and CO_2 conversion in [BMAmm$^+$][TFSI$^-$] for the first time. The EIS parameters in O_2 saturated [BMAmm$^+$][TFSI$^-$] were different from those detected in O_2/CO_2 saturated [BMAmm$^+$][TFSI$^-$] or CO_2 saturated [BMAmm$^+$][TFSI$^-$]. This was rationalized to be due to the formation of a [BMAmm$^+$][TFSI$^-$] film on the GC electrode, creating a 2.031 × 10^{-9} μF cm^{-2} double-layer capacitance (C_{DL}). Therefore, during the $O_2^{\bullet-}$ generation and CO_2 utilization in [BMAmm$^+$][TFSI$^-$], the C_{DL} increased to 5.897 μF cm^{-2} and 7.763 μF cm^{-2}, respectively. The CO_2 in [BMAmm$^+$][TFSI$^-$] was found to be highly unlikely to be electrochemically converted due to the high charge transfer resistance of 6.86 × 10^{18} kΩ. Subsequently, $O_2^{\bullet-}$ directly mediated the CO_2 conversion through a nucleophilic addition reaction pathway. These results offer new and sustainable opportunities for utilizing CO_2 by reactive oxygen species in ionic liquid media.

Received 16th September 2020,
Accepted 30th November 2020

DOI: 10.1039/d0cp04903d

rsc.li/pccp

1. Introduction

The global abundance of CO_2 is estimated to be more than 550 ppm in the next 3–8 decades mainly due to the high levels of anthropogenic activities.[1] As of 2020, the amount of CO_2 in the atmosphere is 420 ppm and this can disrupt the conventional climate cycle, thereby increasing the chance of harsh weather.[2] To combat this deviation from the 350 ppm equilibrium threshold of global CO_2 levels, international and governmental agencies have agreed to cut down 90% of global CO_2 emission through capture and utilization techniques.[3,4] The utilization of CO_2 entails a strategic change in its chemical stability ($\Delta G^{\circ}_{fCO_2} = -396$ kJ mol^{-1}), with the resultant formation of the desired product.[5] Also, sucking one ton of CO_2 directly from the atmosphere as a capture technique costs about $94–232.[6] This indicates that CO_2 is apparently a relatively inexpensive C-1 feedstock for the synthesis of a variety of commodity chemical products.

In the utilization of CO_2, the main focus is on the alteration of the 4+ oxidation state of C(sp). Accordingly, many catalytic conversions of CO_2 into fuels and drop-in fuels, such as electrochemical,[7] thermochemical,[8] and photochemical[9] means, have been investigated. Further utilization of CO_2 as a cheap C-1 feedstock has been reported to produce carbon

[a] *Department of Chemical Engineering, University of Malaya, Kuala Lumpur, 50603, Malaysia. E-mail: ryusoff@um.edu.my*
[b] *University of Malaya Centre for Ionic Liquids (UMCiL), University of Malaya, Kuala Lumpur 50603, Malaysia. E-mail: maan_hayyan@yahoo.com*
[c] *Chemical Engineering Program, Faculty of Engineering and Technology, Muscat University, P. O. Box 550, Muscat, P.C. 130, Oman*
[d] *Centre for Carbon Dioxide Capture and Utilization (CCDCU), School of Engineering and Technology, Sunway University, Bandar Sunway, 47500 Petaling Jaya, Malaysia. E-mail: kheireddinea@sunway.edu.my*
[e] *Department of Engineering, Lancaster University, Lancaster, LA1 4YW, UK*

† Electronic supplementary information (ESI) available. See DOI: 10.1039/d0cp04903d

nanotubes (CNTs) as a 100-fold cheaper option than the conventional chemical vapor deposition.[10–12] Other electrochemical CO_2 utilization techniques largely produce oxocarbons.[13–15] Recently, we reported the production of peroxydicarbonate ($C_2O_6^{2-}$) as an oxocarbon which serves as a carboxylating agent.[16] Quantum chemical computations were employed to gain insights toward the most probable interactions of the molecules mediated by superoxide ion ($O_2^{\bullet-}$), and the subsequent formation of $C_2O_6^{2-}$. To support possible scale-up, understanding the mechanism that governs the process of CO_2 conversion either to oxocarbons, fuels or commodity chemicals is mandatory. In general accounts regarding CO_2 utilization by $O_2^{\bullet-}$ or any conventional means, this is a major drawback that could limit CO_2 conversion. Especially when using $O_2^{\bullet-}$ to promote CO_2 conversion, a medium that could capture CO_2 and sustainably retain $O_2^{\bullet-}$ for utilization is desired. Due to the intriguing properties of ionic liquids (ILs) such as the large electrochemical potential window, high ionic conductivity, strong thermal and chemical stability, and low vapour pressure, they have been used to capture CO_2 during electrochemical conversion.[17–21] In addition, the solubility of CO_2 and O_2 in ILs is high.[22–24] These IL properties facilitate direct electrochemical conversion of O_2 and CO_2 even under ambient conditions.[16,25–27] Also, ILs are suitable media for generation of $O_2^{\bullet-}$ mainly due to their capacity to hold radicals for a sustained period of time.[16,28–35] The kinetics of $O_2^{\bullet-}$ in ILs fall in the range of $\sim 10^{-5}$ to 10^{-3} s^{-1}, indicating that $O_2^{\bullet-}$ can exhibit noticeable long-term stability.[31,36–38] The composition of ILs also plays a primary role. For instance, it was reported that imidazolium-based ILs react with $O_2^{\bullet-}$ to produce the corresponding 2-imidazolones.[35,39,40] This is an indication that the electrochemistry of O_2 to generate and implement $O_2^{\bullet-}$ is strongly influenced by the nature of the IL-cation.[41]

Ammonium based ILs are renown to be stable to nucleophilic attack by $O_2^{\bullet-}$ unlike imidazolium-based ILs.[31] It was found that the C(sp) in the trimethyl-*n*-hexylammonium [$TMHAmm^+$] cation is negative, while the carbons at the 2-, 4- and 5-positions in 1-ethyl-3-methylimidazolium [$EMIm^+$], and 1,2-dimethyl-3-propylimidazolium [$DMPIm^+$] are positive.[42–44] In principle, negatively charged atoms are less susceptible to the nucleophilic influence of $O_2^{\bullet-}$, unlike positively charged atoms.[45] Stable ILs are required in the promotion of $O_2^{\bullet-}$ driven catalysis, particularly for CO_2 conversion.[16,29] Most CO_2 conversions mediated by $O_2^{\bullet-}$, especially in ILs, are limited by the need of unravelling the mechanism of the process.[29] Therefore, this is an inherent challenge that needs to be addressed.[46]

This work is a major advance of our earlier study, which centred on the use of COSMO-RS and Gaussian calculations to unravel the fundamental mechanistic understanding of the transformation of CO_2 by electro-generated $O_2^{\bullet-}$ to produce $C_2O_6^{2-}$.[16] The experimental electrochemical impedance spectroscopy approach was employed for the first time to understand the mechanism of CO_2 utilization by $O_2^{\bullet-}$ in an IL to result in $C_2O_6^{2-}$ generation. COSMO-RS and quantum chemical calculations using the COSMOthermX and Gaussian 09 software packages were also conducted as a necessary guideline to gain insights on the fundamental chemical properties of the molecular architecture of $O_2^{\bullet-}$/ILs/CO_2 and O_2. Then, $O_2^{\bullet-}$ was electrochemically generated and utilized for conversion of CO_2 in butyltrimethylammonium bis(trifluoromethylsulfonyl)imide [$BMAmm^+$][$TFSI^-$]. The long-term stability of $O_2^{\bullet-}$ in [$BMAmm^+$][$TFSI^-$] was confirmed using the UV-vis irradiation kinetics of dynamic $O_2^{\bullet-}$ degradation. [$BMAmm^+$][$TFSI^-$] is structurally different from the ones reported in the literature,[31] considering that it is made of negatively charged carbon atoms, which was found as suitable medium for sustainable generation of $O_2^{\bullet-}$. Although many reports showed electrochemical reduction of O_2 to $O_2^{\bullet-}$ in other ILs,[31] we are not aware of any study that has elucidated the mechanism of O_2 reduction to $O_2^{\bullet-}$ therein, and subsequent utilization of CO_2.

2. Materials and methods

2.1 Materials

The ILs used in this study were butyltrimethylammonium bis(trifluoromethylsulfonyl)imide [$BMAmm^+$][$TFSI^-$] (purity ≥99%, IOLITEC) and 1-ethyl-3-methylimidazolium bis(trifluoromethylsulfonyl)imide [$EMIm^+$][$TFSI^-$] (purity ≥98%, Sigma Aldrich). These ILs were selected following the geometry guideline in our previous studies, which provided capacity for stable $O_2^{\bullet-}$ generation.[16,31,32,34,47,48] These were all obtained with <1% moisture content, which was determined using a Karl Fischer titrator (V30S). The IL structures are presented in Scheme 1. Dimethylsufoxide (DMSO; purity ≥99.97%) was purchased from Fisher Chemicals. Potassium superoxide (KO_2, purity ≥99.9%) was purchased from Sigma Aldrich. Throughout the experiment, ultra-high purity gases N_2 (purity ≥99.999%), and O_2 (purity ≥99.999%) were used as purchased from Gaslink SDN Malaysia.

2.2 Computational analysis

2.2.1 COSMO-RS analysis. COSMO-RS analysis using the latest COSMOthermX software package was conducted based on BP-TZVP-C30-1401-ctd parameterization.[49] In a typical procedure, the [$BMAmm^+$][$TFSI^-$], [$EMIm^+$][$TFSI^-$] control, $O_2^{\bullet-}$,

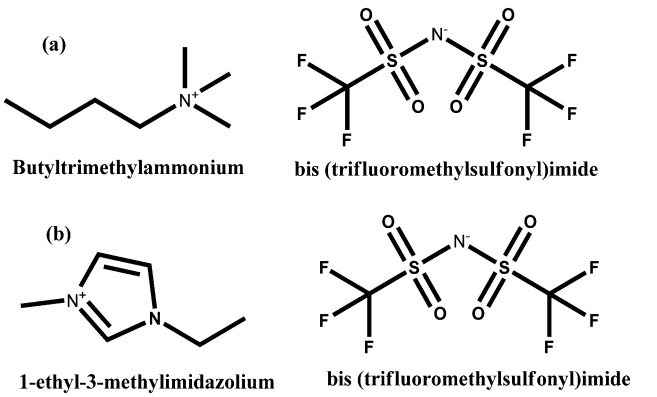

Scheme 1 Structures of (a) [$BMAmm^+$][$TFSI^-$] and (b) [$EMIm^+$][$TFSI^-$]

O_2, and CO_2 geometries were first built and optimized with the Tmolex software package based on the Hartree–Fock level of theory and def-SV(P) basis set.[50] The IL-anion bis(trifluoromethylsulfonyl)imide ([$TFSI^-$]) exists in the latest COSMOthermX database. Therefore, it was isolated and used without further treatment, but the COSMO-files of other molecules were generated at the DFT level of theory using the Beck–Perdew-86 functional.[51] During the generation of the COSMO-files, the zeta valence potential (def-TZVP) basis set[52] was used. After generating the COSMO-files for [$BMAmm^+$][$TFSI^-$], the [$EMIm^+$][$TFSI^-$] control, $O_2^{\bullet-}$, O_2, and CO_2, the job functional for a molecular mixture in COSMOthermX was sought to produce the most probable interaction among the molecules. Consequently, their σ-profiles and surfaces were isolated as additional outputs.

2.2.2 Global electrophilicity index. The geometry of [$BMAmm^+$], the [$EMIm^+$] control, $O_2^{\bullet-}$, and CO_2 was optimized in the ground state using the Hartree–Fock level of theory using the singlet default spin mode and 3-21G basis set in the Gaussian 09 software.[53] To extract their respective highest occupied molecular orbital (HOMO) and lowest unoccupied molecular orbital (LUMO), further energy analysis at the same level of theory was conducted on the optimized geometries. New molecular orbitals were updated and the respective molecular orbitals were visualized in terms of molecular orbital cubes. The HOMO and LUMO energies were used to calculate the chemical hardness (η) and chemical potential (μ) from eqn (1) and (2), respectively.[54] Eventually, using eqn (3),[54,55] the global electrophilicity indices (ω) were computed.

$$\eta = \frac{1}{2}(E_{LUMO} - E_{HOMO}) \quad (1)$$

$$\mu = \frac{1}{2}(E_{HOMO} + E_{LUMO}) \quad (2)$$

$$\omega = \frac{\mu^2}{2\eta} \quad (3)$$

where η = chemical hardness, μ = global electronic chemical potential, and ω = electrophilicity index.

2.3 Electrochemical impedance spectroscopy (EIS)

EIS measurements of [$BMAmm^+$][$TFSI^-$] and [$EMIm^+$][$TFSI^-$] media were performed in galvanostatic mode using a three-electrode system in an aluminium foil Faraday cage present in a glove box with an N_2 environment. The three electrodes are glassy carbon (GC): OD: 6 mm, ID: 3 mm, platinum (Pt): 5.7 cm, BAS Inc., and Ag/AgCl: 6 mm. A sine amplitude of 100 μA in a frequency range of 100 kHz to 100 mHz was used during the measurement. To investigate the mechanism of radical driven catalysis, EIS measurements were conducted in O_2-saturated [$BMAmm^+$][$TFSI^-$] and O_2/CO_2-saturated [$BMAmm^+$][$TFSI^-$] in potentiostatic mode using the same set of electrodes at a 10 mV amplitude. The total harmonic distortion of the AC signal in [$BMAmm^+$][$TFSI^-$] and [$EMIm^+$][$TFSI^-$] was determined.

2.4 Electrochemical generation of $O_2^{\bullet-}$

[$BMAmm^+$][$TFSI^-$] and [$EMIm^+$][$TFSI^-$] were vacuum dried for ~6 h at a temperature of ~50 °C as a form of purification step. One mL of the IL was poured into an electrochemical cell. The GC, Pt and Ag/AgCl electrodes were clamped therein and placed in a sterile jacketed cell kept in a glove box with an N_2 environment. These electrodes were connected to an Autolab potentiostat model PGSTAT302N. The latest Nova 2.1 data acquisition software through a computer was used to control the electrochemical process taking place in the cell. During the process, N_2 was first directed to the electrochemical cell through a gas channel, ensuring an inert environment. Then, O_2 was sparged and cyclic voltammetry (CV) measurements were conducted in the jacketed three-electrode system. In accordance, the charge transfer coefficient (α) governing the process, solubility (C_0) and diffusion coefficient (D_0) of O_2 in the IL were determined using eqn (4)–(6),[34] after chronoamperometry analysis using an ~11 ± 2 μm (dia.) carbon fiber ultra-microelectrode.

$$i_p = (2.99 \times 10^5)\sqrt{\alpha D_0 \nu A^2 C_0^2} \quad (4)$$

$$E_p = E^{0'} - \frac{RT}{\alpha F}\left[0.782 + \ln\left(\frac{D_0^{1/2}}{k^\circ}\right) + \ln\left(\frac{\alpha F}{RT}\right)^{1/2}\right] \quad (5)$$

$$i_{ss} = 4nFD_0C_0r_0 \quad (6)$$

where

i_p = cathodic peak current (A),
i_{ss} = steady-state current (A),
α = charge transfer coefficient,
A = surface area of the macro-working electrode (cm^2),
C_0 = bulk concentration of O_2 (mol mL^{-1}),
D_0 = diffusion coefficient of O_2 (cm^2 s^{-1}),
ν = potential sweep rate (V s^{-1}),
E_p = peak potential for the cathodic current (V),
E° = formal potential of the reaction (V),
R = universal gas constant (J mol^{-1} K),
T = absolute temperature (K),
F = Faraday's constant (96 485 C mol^{-1}),
k° = standard heterogeneous rate constant (cm s^{-1}),
n = number of electrons,
r_0 = radius of the ultra-microelectrode,
I = current (A),
t = time (s).

2.5 Long-term stability of $O_2^{\bullet-}$ in DMSO containing the IL

The long-term stability was tested as described earlier.[32,47] A UV-vis spectrophotometer (PerkinElmer-Lambda 35) was used to measure the absorption spectra of $O_2^{\bullet-}$. Initially, DMSO, [$BMAmm^+$][$TFSI^-$], and [$EMIm^+$][$TFSI^-$] were vacuum dried overnight at 60 °C. In addition, KO_2 was placed in an air tight container with molecular sieves. The KO_2 was transferred into the DMSO and the superoxide chemically generated therein was calibrated. A blank solution of ~0.05 g of the IL in ~5 mL

DMSO was prepared after making ~0.05 g stock of the IL in a closed vial. This was followed by preparing a fresh solution of KO_2 in DMSO. The UV-vis for the blank and 5 mL of KO_2 in 0.05 g IL/DMSO solution was measured immediately by repeating the scans for 180 min steps for [BMAmm$^+$][TFSI$^-$] and [EMIm$^+$][TFSI$^-$] media. The kinetics of $O_2^{\bullet-}$ in these media were determined and the reaction rate constant was evaluated. The long-term stability of $O_2^{\bullet-}$ in DMSO containing the IL was then monitored.

2.6 Utilization of CO_2 by $O_2^{\bullet-}$

The utilization of CO_2 by $O_2^{\bullet-}$ was measured at ambient temperature in a three-electrode cell, containing a GC working electrode, Pt counter electrode and Ag/AgCl reference electrode present in a glove box with an N_2 environment. In a cyclic voltammetry experiment, 1.0 mL of [BMAmm$^+$][TFSI$^-$] was systematically sparged with N_2 to expel any available impurities. Therefore, a 0.1 L min^{-1} flow of O_2 and 0.034 mPa of CO_2 were administered into the [BMAmm$^+$][TFSI$^-$] batch-wise. The medium was subjected to potentiostatic control (*i.e.*, 0.1 to −1.3 V *vs.* Ag/AgCl) under different sweep rates (*i.e.*, 9 mV s^{-1} to 144 mV s^{-1}) during cyclic voltammetry.

3. Results and discussion

3.1 COSMO-RS analysis

Fig. 1 shows the σ-profiles of the [BMAmm$^+$] and [EMIm$^+$] IL-cation compared with the σ-profiles of [TFSI$^-$], O_2, $O_2^{\bullet-}$ and CO_2. The possible non-covalent interactions of the molecules and ions can be estimated through the σ-profiles from COSMO-RS analysis.[56] In general, the σ-profiles are classified within three possible sections based on the charge density measured in units of e nm^{-2} or e Å^{-2}.[57] In this section, we are adopting the measurements in units of e nm^{-2} throughout. Therefore, in the first section of the σ-profiles, the molecule's hydrogen bond donor (HBD) capacity can be assessed at $\sigma <$ −0.820 e nm^{-2}. Accordingly, from Fig. 1a, the HBD behaviour in [BMAmm$^+$][TFSI$^-$] occurred at −0.904 e nm^{-2}, which could be due to the contribution from the C–H group.[58,59] Similarly, the HBD behaviour in CO_2 (σ = −1.040 e nm^{-2}) originates from the positive character of the carbon in CO_2 with sp hybridization that is hydrogen-like, and potentially avails an interaction with $O_2^{\bullet-}$. The second section within the σ-profile is a non-polar region that occurs within the range of −0.820 e nm^{-2} $< \sigma <$ +0.820 e nm^{-2}. [BMAmm$^+$][TFSI$^-$] (Fig. 1a) and the control [EMIm$^+$][TFSI$^-$] (Fig. 1b) have a non-polar range at −0.384 e nm^{-2} and −0.188 e nm^{-2}, respectively. Also, the non-polar range for O_2 and CO_2 was −0.084 e nm^{-2} and +0.328 e nm^{-2}, respectively. These non-polar regions signify where the molecules have their electrons distributed more symmetrically and do not possess an abundance of charges at their opposite sides.[60] The third section, which occurred at $\sigma >$ +0.820 e nm^{-2}, represents the hydrogen bond acceptor (HBA) region. This region was isolated for $O_2^{\bullet-}$ at +1.660 to 2.340 e nm^{-2}. For [TFSI$^-$], the HBA region occurs at +0.912 e nm^{-2} due to the presence of oxygen or fluorine in the molecular structure of the anion. Generally, the HBA plays a crucial role in establishing a bond with HBD species.[61,62] However, since CO_2 and [BMAmm$^+$] have HBDs, then $O_2^{\bullet-}$ has the potential to interact with their HBDs, considering no other strong competitive counter effects.

3.2 Frontier molecular orbital (FMO) analysis

One of the best theories to describe the chemical stability of a molecule is the FMO theory of the highest occupied molecular orbital (HOMO) and lowest unoccupied molecular orbital (LUMO).[63] Considering [BMAmm$^+$], [EMIm$^+$], CO_2, and $O_2^{\bullet-}$, their HOMO and LUMO 3D renderings in terms of the isovalue surface are shown in Fig. 2a–d. These HOMOs and LUMOs may provide valuable data on the energy distribution and behavior of the molecules. There are two scenarios for the ground state HOMO or LUMO regarding these molecules: (1) symmetric isovalue surfaces, where the sizes of the green and brown 3D renderings are the same, and (2) asymmetric isovalue surfaces, where the sizes of the green and red 3D renderings are not the same. The green-colored 3D rendering represents a negative isovalue surface, while the brown-colored rendering represents a positive isovalue surface. These isovalue surfaces define the geometry of the IL molecules especially when their electron densities are rendered as colored 3D objects.[64,65] Therefore, from Fig. 2a, the HOMO of [BMAmm$^+$] with both negative and

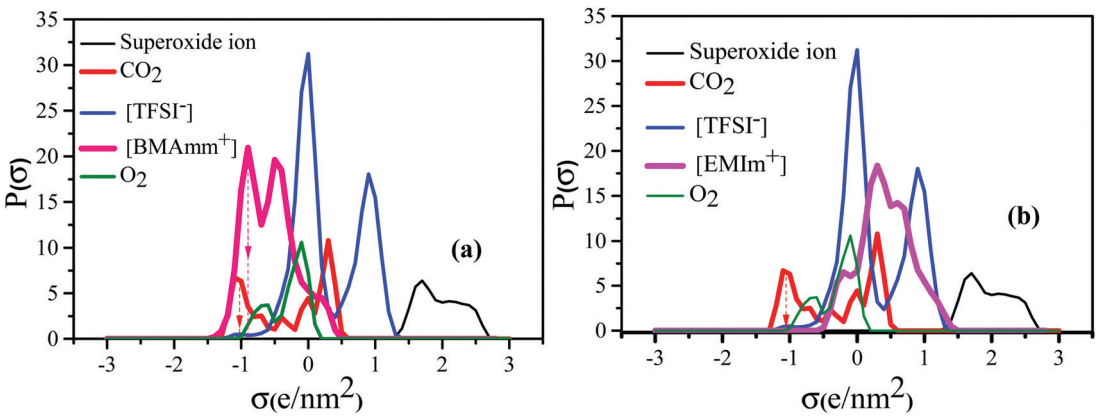

Fig. 1 COSMO RS analysis showing the σ-profile of (a) [BMAmm$^+$] and (b) [EMIm$^+$] IL-cations compared with [TFSI$^-$], O_2, $O_2^{\bullet-}$ and CO_2.

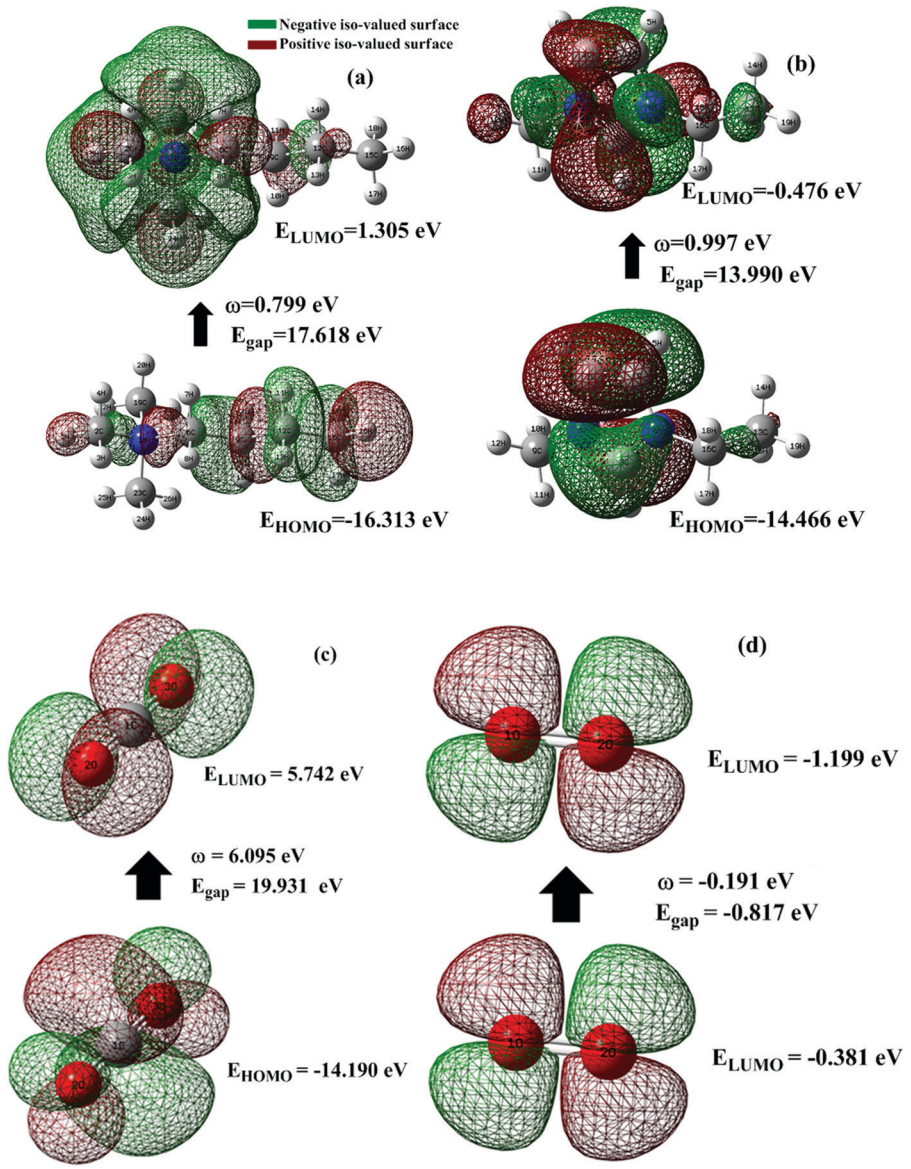

Fig. 2 Frontier molecular orbital showing the 3-D rendered isovalue surface for (a) [BMAmm$^+$] and (b) [BMIm$^+$], (c) CO_2 and (d) $O_2^{\bullet-}$. The green color coding signifies a negative isovalue surface while the brown color coding signifies a positive isovalue surface at the Hartree–Fock/3-21G level of theory.

positive isovalue surfaces is distributed across the IL-cation, excluding $(-CH_3)_2$ that is linked to the nitrogen. The positive (colored brown) and negative (colored green) isovalue surfaces are symmetrical. The LUMO of [BMAmm$^+$] is different from the HOMO of [BMAmm$^+$]. The LUMO is distributed all over [BMAmm$^+$] excluding (CH_3). However, the negative isovalue surface is larger than the positive isovalue surface, and hence they are asymmetrical. Considering [EMIm$^+$] in Fig. 2b, the HOMO and LUMO have an almost symmetrical distribution of either the positive or negative isovalue surface. In the HOMO, the shape is not majorly different from the LUMO. This kind of symmetrical distribution of the HOMO and LUMO isovalue surface can be seen for $O_2^{\bullet-}$ and CO_2, as shown in Fig. 2c and d.

The HOMO energy represents the possible ionization potential, while the LUMO energy represents the electron affinity. In accordance, a high HOMO energy corresponds to a more reactive molecule with electrophiles while a low LUMO energy signifies a less reactive molecule with nucleophiles.[66] The difference between the HOMO and LUMO energies represents the energy gap ($E_{HOMO} - E_{LUMO} = \Delta E_g$), which dictates the chemical reactivity and kinetic stability of molecules.[67] According to Fig. 2a and b, ΔE_g for [BMAmm$^+$] (17.618 eV) is greater than ΔE_g for [EMIm$^+$] (13.990 eV). This implied that [BMAmm$^+$] has less polarization with higher molecular stability. Similarly, as shown in Fig. 2c and d, ΔE_g for CO_2 (19.931 eV) is greater than ΔE_g for $O_2^{\bullet-}$ (−0.817). This implied that $O_2^{\bullet-}$, which has a lower value of ΔE_g than CO_2, [EMIm$^+$], and [BMAmm$^+$], has more polarization with low ionic stability.

However, further estimation of the electrophilicity index showed that [EMIm$^+$] has a more positive character than [BMAmm$^+$]. This is because the electrophilicity index of [EMIm$^+$] is ω = 0.977 eV at the Hartree–Fock/3-21G level of theory, while that of

[BMAmm$^+$] is ω = 0.799 eV at the same level of theory. Also, CO_2 has a more positive character than [EMIm$^+$] and [BMAmm$^+$], judging from its electrophilicity index, which is ω = 19.931 eV. The high value of the electrophilicity index makes the ion more electrophilic and susceptible to attack by $O_2^{\bullet-}$.[16] To precisely confirm the degree of the positive character of [BMAmm$^+$], [EMIm$^+$], or CO_2, further extraction of their Mulliken atomic charge distribution was carried out at the Hartree–Fock//3-21G level of theory. The Mulliken atomic charges, shown in Fig. S1a (ESI†), indicate that all the carbon atoms in [BMAmm$^+$] are negative. In Fig. S1b (ESI†), C(sp^2) in the imidazole ring of [EMIm$^+$] has a +0.642 e a.u.$^{-2}$ Mulliken atomic charge. Also in Fig. S1c (ESI†), C(sp) in CO_2 has a +1.083 e a.u.$^{-2}$ Mulliken atomic charge. These Mulliken atomic charges are insightful to probe the chemical process capability of the molecules.[68,69] This could rationalize why [BMAmm$^+$] has a large negatively charged isovalue surface while [EMIm$^+$] has a more positive character.

3.3 Electrochemical impedance spectroscopy analysis

Fig. S2a and b (ESI†) show the total harmonic distortion profile and a sinusoidal profile of the voltage for the EIS measurement with GC in [BMAmm$^+$][TFSI$^-$] *vs.* Ag/AgCl, respectively. In the [BMAmm$^+$][TFSI$^-$] medium, the total harmonic distortion ranged from 0 to 14% and signified that the medium was stable enough to provide at least 86% undistorted electrical power flow. This is confirmed from the sinusoidal pattern shown in Fig. S2b (ESI†). Accordingly, Fig. S2c (ESI†) presents the Nyquist plot, which is used to estimate the resistance of the [BMAmm$^+$][TFSI$^-$] medium. In the Nyquist plot, two semicircles can be seen as indicated in the inset. The first and hidden semicircle represents the integral resistance (R_1) of [BMAmm$^+$][TFSI$^-$].[76,77] The hidden semicircle and the two obvious ones represent the electron transfer process. Based on EIS modelling, the time constant for the hidden semicircle was associated with only the electrolyte ([BMAmm$^+$][TFSI$^-$]) resistance R_1, which was estimated to be $\sim$1277 Ω. The last two semi-circles are associated with the resistive–capacitive (*RC*) circuit.[78] However, the value of R_2 and R_3 was 7.102 kΩ and 20.662 kΩ, respectively. These resistances (*i.e.*, R_2 and R_3) are associated with capacitance C_2 = 19.316 μF cm^{-2} and C_3 = 19.02 μF cm^{-2}, respectively, and they are peculiar to the charge transfer process. Comparing the Nyquist plot for [BMIm$^+$][TFSI$^-$] (Fig. S2d, ESI†), R_1 was 0.364 Ω, and the value of R_2 and R_3 was 12.938 and 1.389 × 10^3 kΩ, respectively. These resistances are also associated with a capacitance of C_2 = 12.008 μF cm^{-2} and C_3 = 17.165 μF cm^{-2}, respectively. Comparing the Nyquist plots for the [BMAmm$^+$][TFSI$^-$] and [EMIm$^+$][TFSI$^-$] media, the charge transfer resistance R_2 is larger in [EMIm$^+$][TFSI$^-$] (*i.e.*, R_2 = 12.938 kΩ) than in [BMAmm$^+$][TFSI$^-$] (*i.e.*, R_2 = 7.102 kΩ). This makes [EMIm$^+$][TFSI$^-$] less suitable compared with [BMAmm$^+$][TFSI$^-$].

3.4 Electrochemical generation of $O_2^{\bullet-}$ in the ILs

Fig. 3 shows the CV waves for the electrochemical generation of $O_2^{\bullet-}$ in [BMAmm$^+$][TFSI$^-$] and [EMIm$^+$][TFSI$^-$] after sparging them with O_2. In Fig. 3a and b, $O_2^{\bullet-}$ is generated in [BMAmm$^+$][TFSI$^-$] and in [EMIm$^+$][TFSI$^-$] at −0.823 V and −0.915 V *vs.* Ag/AgCl, respectively, for a 144 mV s^{-1} sweep rate. As the sweep rate was reduced to 100, 81, 64, 36 and 9 mV s^{-1}, the O_2 reduction potential in [BMAmm$^+$][TFSI$^-$] was −0.825, −0.812, −0.795, −0.777, and −0.747 V *vs.* Ag/AgCl, respectively. Similarly, the O_2 reduction potential in [EMIm$^+$][TFSI$^-$] was −0.908 V, −0.903 V, −0.896 V, −0.888 V, and −0.857 V *vs.* Ag/AgCl at potential sweep rates 100, 81, 64, 36 and 9 mV s^{-1}, respectively. By comparison, the reduction potential of O_2 reduction in [BMAmm$^+$][TFSI$^-$] was lower because the charge transfer resistance was lower in [BMAmm$^+$][TFSI$^-$] (7102 Ω) than that in [EMIm$^+$][TFSI$^-$] (12 938 Ω). In these media, the CV waves for their cathodic and anodic separations, or their cathodic peak (E_p^c) and the half peak potential ($E_{p/2}^c$) separations are higher than 60 mV (Fig. 3a–d and Table S1, ESI†). This implies that the electrochemical process for the generation of $O_2^{\bullet-}$ was irreversible according to the Nicholian criterion.[33,39,70] By implication of the irreversible process, the $O_2^{\bullet-}$ generated was available for further reaction. According to Fig. 3a and b, the reverse oxidation CV waves show that $O_2^{\bullet-}$ generated in [BMAmm$^+$][TFSI$^-$] and in [EMIm$^+$][TFSI$^-$] is stable, regardless of whether the process is diffusion or surface controlled.[16,47] Moreover, comparing the peak current density with the sweep rate as illustrated in Fig. 3c and d, the linear variation postulates that a diffusion controlled process dominates O_2 reduction in the bulk IL medium and this is unlikely on the surface of the electrode.[71,72]

3.5 Long-term stability of $O_2^{\bullet-}$ in DMSO containing the IL

To study the long-term stability of $O_2^{\bullet-}$ in [BMAmm$^+$][TFSI$^-$] and [EMIm$^+$][TFSI$^-$], UV-visible (UV-vis) analysis was employed. UV-vis was carried out with DMSO serving as a supporting medium for [BMAmm$^+$][TFSI$^-$] and [EMIm$^+$][TFSI$^-$]. Accordingly, Fig. 4(a and b) shows the absorbance spectra of $O_2^{\bullet-}$ generated in DMSO containing individually the respective [BMAmm$^+$][TFSI$^-$] and [EMIm$^+$][TFSI$^-$]. The absorbance band for $O_2^{\bullet-}$ in the supported ILs evidently occurs around 250–270 nm.[32,35,73] Therefore, for [BMAmm$^+$][TFSI$^-$], the steady absorbance for $O_2^{\bullet-}$ was at a $\sim$255–259 nm excitation wavelength. Similarly, the steady absorbance for $O_2^{\bullet-}$ in DMSO containing [EMIm$^+$][TFSI$^-$] was obtained at a $\sim$263 nm excitation wavelength. These absorbance spectra decreased slightly with time. The kinetic data associated with this decrease is shown in Table 1. Accordingly, an 8.4% decay of $O_2^{\bullet-}$ radicals was observed in the [BMAmm$^+$][TFSI$^-$]-based medium. On the other hand, at the same duration, a 46.1% decay of $O_2^{\bullet-}$ was observed in the [EMIm$^+$][TFSI$^-$]-based medium. These indicate that [EMIm$^+$][TFSI$^-$] was not a suitable medium to be employed for generating stable $O_2^{\bullet-}$.[31,36,74] The high decay of $O_2^{\bullet-}$ in the [EMIm$^+$][TFSI$^-$]-based medium is consistent with the observation that the [EMIm$^+$] end has more positive character with an electrophilicity index of $\sim$0.997 eV, and a C(sp) Mulliken charge of +0.642 e a.u.$^{-2}$. The estimation of the kinetic rate constant associated with the decay of $O_2^{\bullet-}$ in DMSO containing the respective IL was further used to differentiate the prowess

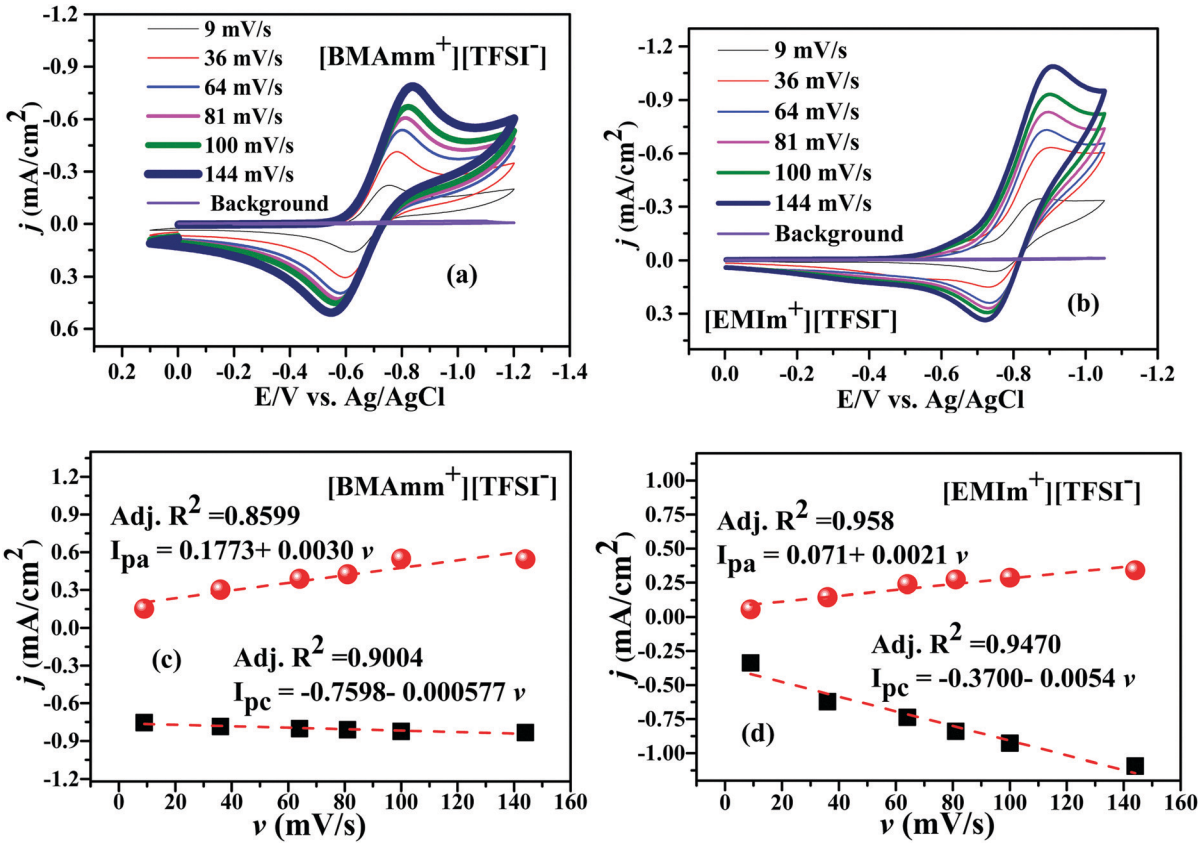

Fig. 3 CVs of $O_2^{\bullet-}$ generation in (a) [BMAmm$^+$][TFSI$^-$] and (b) [EMIm$^+$][TFSI$^-$], and current density against sweep rate in (c) [BMAmm$^+$][TFSI$^-$] and (d) [EMIm$^+$][TFSI$^-$].

of these media. It was found that the $O_2^{\bullet-}$ decay in the [BMAmm$^+$][TFSI$^-$] and [EMIm$^+$][TFSI$^-$]-based media followed a 2nd order reaction and was estimated to be 0.147×10^{-5} and 0.320×10^{-5} M^{-1} s^{-1}, respectively. The $O_2^{\bullet-}$ decay in DMSO containing [BMAmm$^+$][TFSI$^-$] was close to that for $O_2^{\bullet-}$ in DMSO containing [EDMPAmm$^+$][TFSI$^-$] by 9%.[47]

3.6 CO_2 conversion by $O_2^{\bullet-}$ in [BMAmm$^+$][TFSI$^-$]

Considering the high stability of $O_2^{\bullet-}$ in [BMAmm$^+$][TFSI$^-$], it was further used as a medium for CO_2 conversion. The [BMAmm$^+$][TFSI$^-$] was saturated with CO_2 or N_2; on reducing the sweep rate from 144 to 9 mV s^{-1}, a resulting background CV pattern was observed with no visible faradaic current that can be attributed to any redox process taking place (Fig. 5a–f; blue coded-line denoting the blank). This indicates that CO_2 was not electrochemically active and [BMAmm$^+$][TFSI$^-$] contained no electrochemically active impurities. According to Fig. 5(a–f), the CO_2 utilization by $O_2^{\bullet-}$ is evident from the disappearance of the reverse oxidation wave for $O_2^{\bullet-}$ generation when both O_2 and CO_2 are sparged

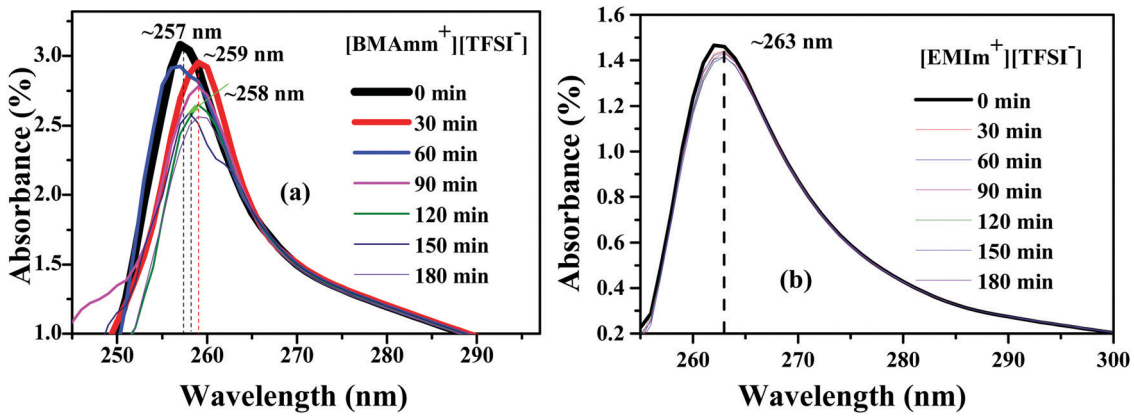

Fig. 4 Absorbance spectra of $O_2^{\bullet-}$ generation in DMSO in the presence of (a) [BMAmm$^+$][TFSI$^-$] and (b) [EMIm$^+$][TFSI$^-$].

Table 1 $O_2/O_2^{\bullet-}$ long-term and short-term stability parameters

IL	2nd order rate constant $\times 10^{-5}$ (M^{-1} s^{-1})	Total consumption % of $O_2^{\bullet-}$	$D_0 \times 10^{10}$ (m^2 s^{-1})	C_0 (mM)	α
[EMIm$^+$][TFSI$^-$]	0.320	46.1	1.830	10.200	0.405
[BMAmm$^+$][TFSI$^-$]	0.147	8.4	1.770	5.590	0.503

in [BMAmm$^+$][TFSI$^-$] electrolyte. This is an indication of spontaneous consumption of CO_2 and $O_2^{\bullet-}$.[16,29] The consumption of CO_2 by $O_2^{\bullet-}$ is in strong agreement with the literature to confirm selective *in situ* production of $C_2O_6^{2-}$ due to the increase in the potential forward reductive peak.[16,75] The forward reductive peak potential was also raised from −0.750 V (*i.e.*, for only $O_2^{\bullet-}$ before $C_2O_6^{2-}$ generation) to −0.806 V *vs.* Ag/AgCl (*i.e.*, after $C_2O_6^{2-}$ generation) for a 9 mV s^{-1} sweep rate. This pattern is similar for other sweep rates, such as 36 mV s^{-1} (−0.784 to −0.855 V), 64 mV s^{-1} (−0.798 to −0.880 V), 81 mV s^{-1} (−0.811 to −0.890 V), 100 mV s^{-1} (−0.825 to −0.900 V), and 144 mV s^{-1} (−0.841 to −0.930 V).

EIS in potentiostatic mode was used to study the mechanism of $O_2^{\bullet-}$ electrogeneration and CO_2 utilization in [BMAmm$^+$][TFSI$^-$] on the GC electrode. In the O_2-saturated-[BMAmm$^+$][TFSI$^-$], CO_2-saturated-[BMAmm$^+$][TFSI$^-$] and

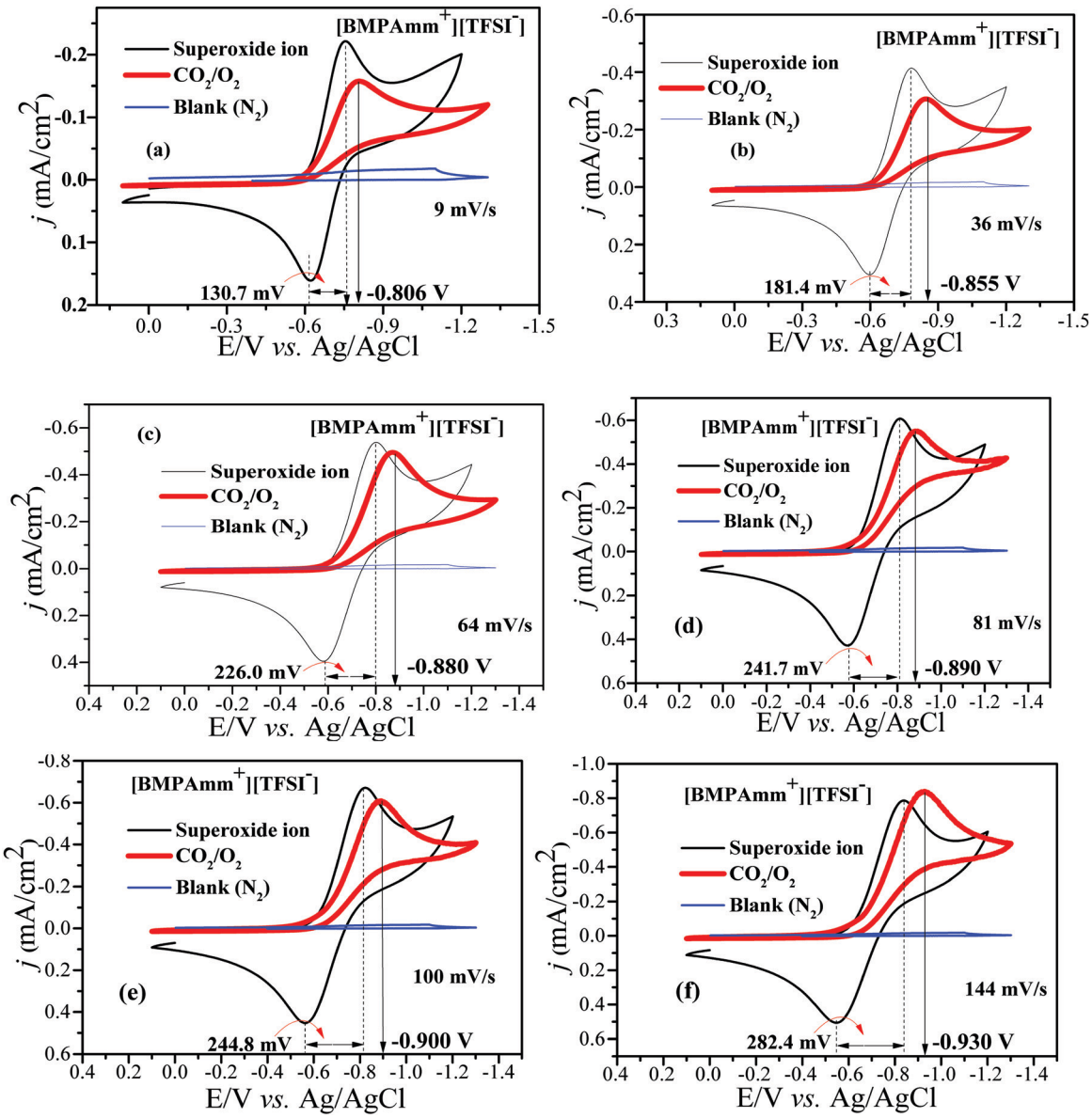

Fig. 5 (a–f) CVs of CO_2 conversion by $O_2^{\bullet-}$ in [BMAmm$^+$][TFSI$^-$] after sparging with N_2 (background), CO_2, O_2, and CO_2/O_2 simultaneously at 27 °C, GC *vs.* Ag/AgCl at various sweep rates.

O_2/CO_2-saturated-[BMAmm$^+$][TFSI$^-$] electrolytes, EIS measurements were conducted at −0.773, −0.360, and −0.360 V *vs.* Ag/AgCl, respectively. The EIS spectra detected in the O_2-saturated-[BMAmm$^+$][TFSI$^-$], CO_2-saturated-[BMAmm$^+$][TFSI$^-$] and O_2/CO_2-saturated-[BMAmm$^+$][TFSI$^-$] electrolytes are presented in Fig. 6. In the O_2-saturated-[BMAmm$^+$][TFSI$^-$] and O_2/CO_2-saturated-[BMAmm$^+$][TFSI$^-$] electrolyte (Fig. 6a and b), the Nyquist plot shows a typical feature: in the high frequency region, a small semi-circle can be observed, which corresponds to the electron transfer process. By contrast, in the low-frequency region, a bigger semi-circle was detected, showing a total of two circles which correspond to two time scales that are associated with the resistor capacitance circuit (EC).[78] The EIS is modelled by a modified Randles EC[79] (Fig. 6a–c), where $R_1 = R_e$ is the electrolyte resistance, $R_2 = R_{ct}$ is the charge transfer, C_2 is the double-layer capacitance and W is the Warburg impedance. The EC is described by four elements corresponding to four impedance parameters. This denotes a system with two time-constants. The low-frequency region detected in CO_2-saturated-[BMAmm$^+$][TFSI$^-$] shows a straight line, Fig. 6c. This pattern is associated with a diffusion limited process.

It was found that R_e varied in the following order: 5.467, 4.378, and 2.116 kΩ for the O_2-saturated-[BMAmm$^+$][TFSI$^-$],

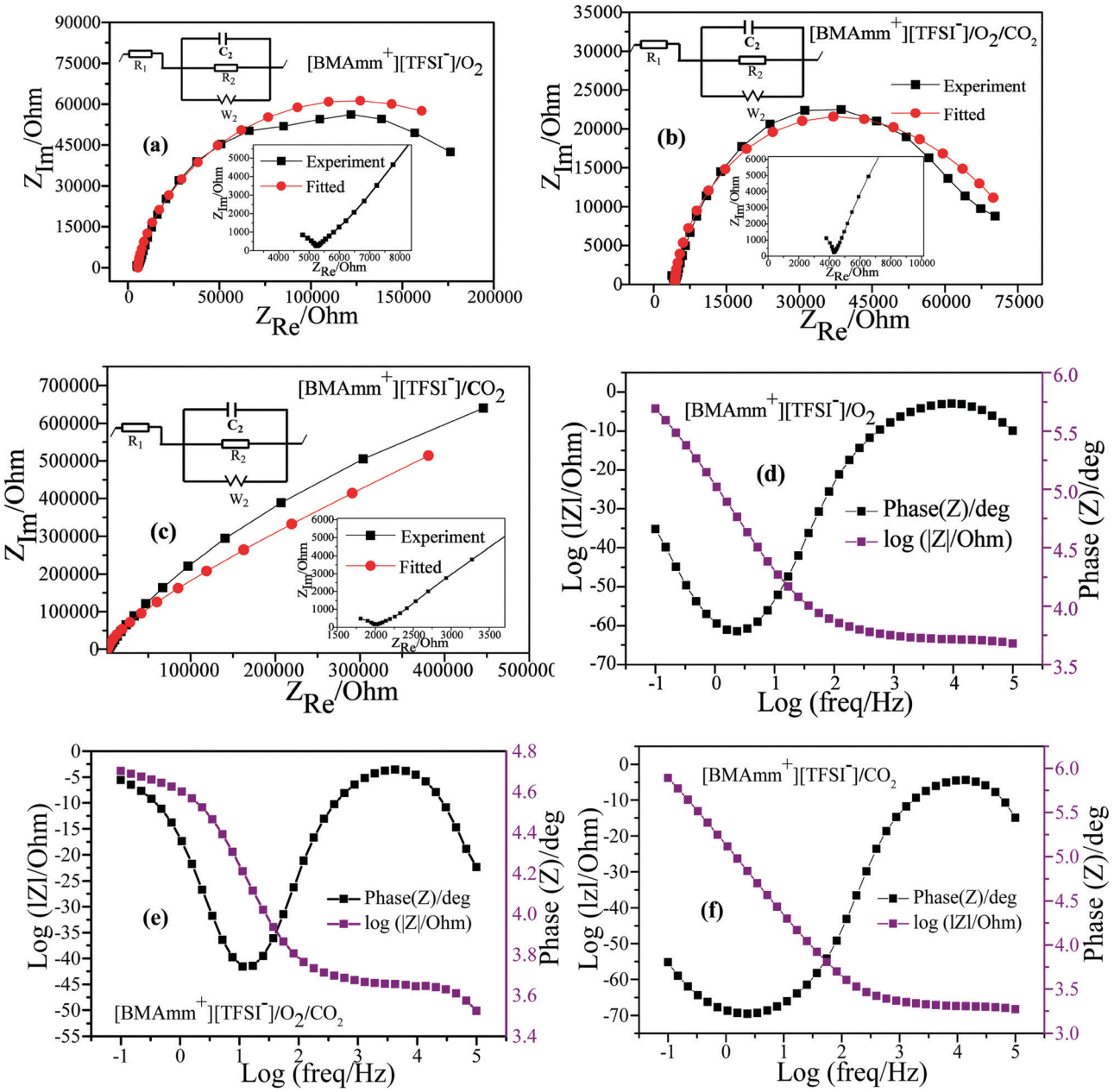

Fig. 6 Nyquist plots detected in (a) O_2-saturated-[BMAmm$^+$][TFSI$^-$], (b) O_2/CO_2-saturated-[BMAmm$^+$][TFSI$^-$] and (c) CO_2-saturated-[BMAmm$^+$][TFSI$^-$]. Bode plots detected in (d) O_2-saturated-[BMAmm$^+$][TFSI$^-$], (e) O_2/CO_2-saturated-[BMAmm$^+$][TFSI$^-$] and (f) CO_2-saturated-[BMAmm$^+$][TFSI$^-$].

Table 2 EIS parameter in the equivalent circuit model

Catholyte	R_e/kΩ	R_{ct}/kΩ	C_2/μF cm^{-2}	W/Ω s$^{1/2}$ cm^2
O_2-saturated-[BMAmm$^+$][TFSI$^-$]	5467	261.467	5.897	293 191
CO_2-saturated-[BMAmm$^+$][TFSI$^-$]	2116	6.86×10^{18}	7.764	426 284
O_2/CO_2-saturated-[BMAmm$^+$][TFSI$^-$]	4378	79.00	7.507	82 444

CO_2-saturated-[BMAmm$^+$][TFSI$^-$], and O_2/CO_2-saturated-[BMAmm$^+$][TFSI$^-$] electrolytes, respectively. The double layer capacitance (C_2) associated with R_e also varies in the following order: 5.897, 7.764, and 7.507 μF cm^{-2} in the respective O_2-saturated-[BMAmm$^+$][TFSI$^-$], O_2/CO_2-saturated-[BMAmm$^+$][TFSI$^-$], and CO_2-saturated-[BMAmm$^+$][TFSI$^-$]. Comparing the double layer capacitance detected in these media, an apparent peculiarity can be observed. This suggests that the mechanism of O_2 reduction to $O_2^{\bullet-}$ and the subsequent CO_2 utilization by $O_2^{\bullet-}$ in these media were associated with different charge mobility. The reasonable explanation is that [BMAmm$^+$][TFSI$^-$] got adsorbed on the surface of the GC electrode to form a thin film layer. By virtue of sparging O_2, CO_2 or O_2/CO_2, the gases are expected to get absorbed by [BMAmm$^+$][TFSI$^-$]. These contributed to different polarizations with a consequence of different double layer capacitances. Further analysis of the charge transfer resistance (R_{ct}) revealed that the process is faster in O_2/CO_2-saturated-[BMAmm$^+$][TFSI$^-$] (R_{ct} = 79 kΩ). This R_{ct} is lower than the ones detected in O_2-saturated-[BMAmm$^+$][TFSI$^-$] (R_{ct} = 261.467 kΩ) or CO_2-saturated-[BMAmm$^+$][TFSI$^-$] ($R_{ct} = 6.86 \times 10^{18}$ kΩ). It can be noticed that the R_{ct} value detected in CO_2-saturated-[BMAmm$^+$][TFSI$^-$] was extremely high. This result can inspire the suggestion that charge mobility therein is almost absent. Therefore, under this condition, CO_2 conversion would not occur but it can be available for direct nucleophilic oxidation by $O_2^{\bullet-}$.

The Bode plots detected in the O_2-saturated-[BMAmm$^+$][TFSI$^-$], CO_2-saturated-[BMAmm$^+$][TFSI$^-$] and O_2/CO_2-saturated-[BMAmm$^+$][TFSI$^-$] electrolytes are shown in Fig. 6d–f. In the O_2-saturated-[BMAmm$^+$][TFSI$^-$] and CO_2-saturated-[BMAmm$^+$][TFSI$^-$] electrolytes, only one peak can be seen and both have a similar frequency response (Fig. 6d and f). By contrast, in O_2/CO_2-saturated-[BMAmm$^+$][TFSI$^-$], there are two peaks (Fig. 6e). These results indicate that the mechanisms of CO_2 utilization by $O_2^{\bullet-}$ and O_2 reduction to $O_2^{\bullet-}$ were different. However, the mechanism of O_2 reduction or any possibility of electrochemical CO_2 reduction may be similar since they both have similar BODE impedance profiles.

The impedance parameters obtained following the fitting of the EIS experimental results by using the equivalent circuits displayed in Fig. 6 are listed in Table 2. It can be observed that the charge transfer resistance detected in CO_2-saturated-[BMAmm$^+$][TFSI$^-$] is significantly higher than the ones observed in the O_2/CO_2-saturated-[BMAmm$^+$][TFSI$^-$] and O_2-saturated-[BMAmm$^+$][TFSI$^-$] electrolytes, indicating that intermediate movement therein may be unlikely. This indicates that CO_2 might be absorbed and remained available for direct interaction with $O_2^{\bullet-}$. These results further confirmed the

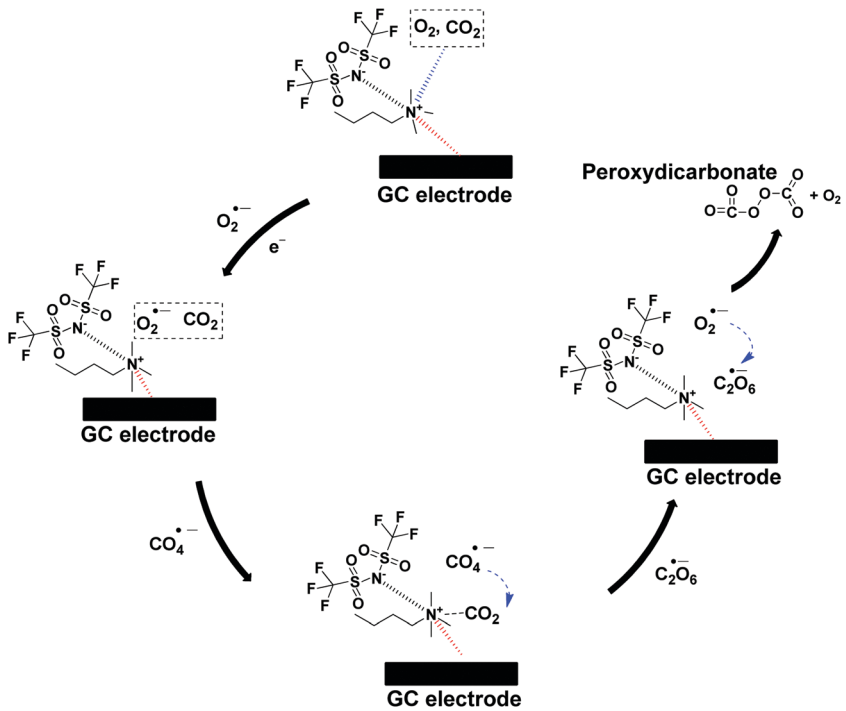

Scheme 2 The proposed mechanism of CO_2 utilization by $O_2^{\bullet-}$ in [BMAmm$^+$][TFSI$^-$].

$O_2^{\bullet-}$ catalyzed CO_2 reduction. Hence, reducing the activation energy and the overpotential of CO_2 reduction can be ascribed to the high charge transfer resistance.

3.7 Catalytic mechanism

The CO_2 utilization by $O_2^{\bullet-}$ in ILs investigated by many researchers necessitates the need to elucidate the proper catalytic mechanism.[16,29,31] Therefore, the mechanism is described as follows: firstly, O_2 and/or CO_2 will diffuse and get absorbed by [$BMAmm^+$][$TFSI^-$] due to the linear σ-profiles of O_2, CO_2 and [$BMAmm^+$][$TFSI^-$] which centered at their non-polar ends with $\sigma = -0.791$ e nm^{-2} to $\sigma = 0.81$ e nm^{-2}, as explained in Section 3.1. Therefore, the O_2-saturated-[$BMAmm^+$][$TFSI^-$], O_2/CO_2-saturated-[$BMAmm^+$][$TFSI^-$] or CO_2-saturated-[$BMAmm^+$][$TFSI^-$] further got momentarily adsorbed on the surface of the GC electrode through participation of the IL moiety to form an IL layer. It was shown that the IL layer could be formed during the electrochemical process occurring in the IL.[80] Then, O_2 will diffuse through the bulk from being absorbed by the [$BMAmm^+$][$TFSI^-$] solution to the vicinity of the GC electrode. O_2 could be possibly transferred through the space between the adsorbed IL layer and the GC electrode surface. Eventually, O_2 gets reduced to $O_2^{\bullet-}$ *via* single electron transfer on the GC electrode. Due to the extremely high charge transfer resistance for CO_2 saturated media, CO_2 will follow a different mechanism (see Table 2), whereas the charge transfer resistance value for O_2/CO_2-saturated-[$BMAmm^+$][$TFSI^-$] was very small (see Table 2). Accordingly, the $O_2^{\bullet-}$ that is electrochemically generated can be postulated to attack the C(sp) center of CO_2, which is highly susceptible because of its positive Mulliken charge (see Fig. S1c, ESI†). During the process, the rate-determining step is the first electron transfer from the cathode to the absorbed O_2 to form the highly-energetic $O_2^{\bullet-}$ radical. The generated $O_2^{\bullet-}$ interacted with CO_2 *via* nucleophilic addition to induce the formation of $CO_4^{\bullet-}$. $CO_4^{\bullet-}$ further followed a consecutive reaction step with CO_2 to form $C_2O_6^{\bullet-}$. In another step of the consecutive reaction between $C_2O_6^{\bullet-}$ and $O_2^{\bullet-}$, $C_2O_6^{2-}$ was formed along with O_2. The reaction summary is presented in Scheme 2. The results are in agreement with the CO_2 conversion by $O_2^{\bullet-}$ in aprotic solvents.[75] The result also revealed a strong advance that $O_2^{\bullet-}$ was undergoing a nucleophilic addition to CO_2 due to the extremely high charge transfer resistance in the CO_2 saturated [$BMAmm^+$][$TFSI^-$]. This rendered CO_2 to be highly unlikely to undergo electrochemical transformation to $CO_2^{\bullet-}$ as conventionally reported.[81] The mechanism of CO_2 conversion by direct addition of $O_2^{\bullet-}$ is observable and plausible because [$BMAmm^+$][$TFSI^-$] was significantly stable for the process due to its large negative isovalue surface, unlike aprotic solvents.

4. Conclusion

[$BMAmm^+$][$TFSI^-$] was successfully used as a task-specific electrolyte for electrochemical $O_2^{\bullet-}$ generation and conversion of CO_2 into $C_2O_6^{2-}$. It was found that large negative isovalue surfaces accrued from negatively charged carbon atoms in ILs like [$BMAmm^+$][$TFSI^-$] could induce them to be less susceptible to attack by $O_2^{\bullet-}$. In contrast, the IL large positive isovalue surfaces accrued from at least one positively charged carbon atom such as in the case of [$EMIm^+$] can induce them to become more susceptible to attack by $O_2^{\bullet-}$. The consequence of $O_2^{\bullet-}$ susceptibility can be measured quantitatively using the long-time stability from UV-vis irradiation analysis. Accordingly, it was noticed that the [$BMAmm^+$] based IL recorded significant $O_2^{\bullet-}$ long-time stability by allowing only 8.4% decay. This rendered the IL a suitable medium for a radical driven CO_2 utilization process. Moreover, the $C_2O_6^{2-}$ produced in the [$BMAmm^+$][$TFSI^-$] medium was detected by the total disappearance of the oxidative faradaic current for the $O_2^{\bullet-}/O_2$ couple. Therefore, the mechanism of CO_2 utilization by $O_2^{\bullet-}$ is limited by O_2 electrochemical reduction to $O_2^{\bullet-}$. The CO_2 was found to be electrochemically stable due to the high charge transfer resistance in CO_2 saturated [$BMAmm^+$][$TFSI^-$]. It is expected that this work will open more research opportunities toward using ILs as promising media for electrochemical reactions and applications of $O_2^{\bullet-}$ in organic synthesis of speciality chemicals or drop-in fuel molecules. The study can also serve as a protocol toward the use of different IL media in unraveling the chemistry of reactive oxygen species and their industrial relevance.

Conflicts of interest

There are no conflicts to declare.

Acknowledgements

The authors would like to express their gratitude to the Newton Fund Institutional Links Project (IF013-2015) and RU Grant (GPF058A) for financial support throughout this research.

References

1 M. R. Smith and S. S. Myers, *Nat. Clim. Change*, 2018, **8**, 834–839.
2 R. J. Kuhns and G. H. Shaw, *Navigating the Energy Maze*, Springer, 2018, pp. 99–115.
3 C. J. Rhodes, *Sci. Prog.*, 2016, **99**, 97–104.
4 A. A. Fawcett, G. C. Iyer, L. E. Clarke, J. A. Edmonds, N. E. Hultman, H. C. McJeon, J. Rogelj, R. Schuler, J. Alsalam and G. R. Asrar, *Science*, 2015, **350**, 1168–1169.
5 J. Li, O. Sode, G. A. Voth and S. Hirata, *Nat. Commun.*, 2013, **4**, 2647.
6 J. Tollefson, *Nature*, 2018, **558**, 173.
7 S. Nitopi, E. Bertheussen, S. B. Scott, X. Liu, A. K. Engstfeld, S. Horch, B. Seger, I. E. L. Stephens, K. Chan, C. Hahn, J. K. Nørskov, T. F. Jaramillo and I. Chorkendorff, *Chem. Rev.*, 2019, **119**, 7610–7672.
8 J. Artz, T. E. Müller, K. Thenert, J. Kleinekorte, R. Meys, A. Sternberg, A. Bardow and W. Leitner, *Chem. Rev.*, 2018, **118**, 434–504.

9 J. L. White, M. F. Baruch, J. E. Pander, Y. Hu, I. C. Fortmeyer, J. E. Park, T. Zhang, K. Liao, J. Gu, Y. Yan, T. W. Shaw, E. Abelev and A. B. Bocarsly, *Chem. Rev.*, 2015, **115**, 12888–12935.
10 J. Ren and S. Licht, *Sci. Rep.*, 2016, **6**, 27760.
11 J. Ren, M. Johnson, R. Singhal and S. Licht, *J. CO_2 Util.*, 2017, **18**, 335–344.
12 S. Licht, *J. CO_2 Util.*, 2017, **18**, 378–389.
13 D. R. Kauffman, J. Thakkar, R. Siva, C. Matranga, P. R. Ohodnicki, C. Zeng and R. Jin, *ACS Appl. Mater. Interfaces*, 2015, **7**, 15626–15632.
14 F.-Y. Gao, R.-C. Bao, M.-R. Gao and S.-H. Yu, *J. Mater. Chem.*, 2020, **8**, 15458–15478.
15 D. L. T. Nguyen, Y. Kim, Y. J. Hwang and D. H. Won, *Carbon Energy*, 2020, **2**, 72–98.
16 A. Halilu, M. Hayyan, M. K. Aroua, R. Yusoff and H. F. Hizaddin, *ACS Appl. Mater. Interfaces*, 2019, **11**, 25928–25939.
17 A. Aljuhani, M. R. Aouad, N. Rezki, O. A. Aljaldy, S. A. Al-Sodies, M. Messali and I. Ali, *J. Mol. Liq.*, 2019, **285**, 790–802.
18 S. K. Singh and A. W. Savoy, *J. Mol. Liq.*, 2020, **297**, 112038.
19 I. Ali, M. Suhail, M. M. Sanagi and H. Y. Aboul-Enein, *Crit. Rev. Anal. Chem.*, 2017, **47**, 332–339.
20 A. Hussain, M. F. AlAjmi, I. Hussain and I. Ali, *Crit. Rev. Anal. Chem.*, 2019, **49**, 289–305.
21 M. Kissoudi and V. Samanidou, *Molecules*, 2018, **23**, 1437.
22 I. Bahadur, K. Osman, C. Coquelet, P. Naidoo and D. Ramjugernath, *J. Phys. Chem. B*, 2015, **119**, 1503–1514.
23 J. L. Anthony, J. L. Anderson, E. J. Maginn and J. F. Brennecke, *J. Phys. Chem. B*, 2005, **109**, 6366–6374.
24 J. L. Anderson, J. K. Dixon and J. F. Brennecke, *Acc. Chem. Res.*, 2007, **40**, 1208–1216.
25 S. Zeng, X. Zhang, L. Bai, X. Zhang, H. Wang, J. Wang, D. Bao, M. Li, X. Liu and S. Zhang, *Chem. Rev.*, 2017, **117**, 9625–9673.
26 K. Seo, C. Tsay, B. Hong, T. F. Edgar, M. A. Stadtherr and M. Baldea, *ACS Sustainable Chem. Eng.*, 2020, **8**, 10242–10258.
27 Y. Zhang, S. Zhang, X. Lu, Q. Zhou, W. Fan and X. Zhang, *Chem. – Eur. J.*, 2009, **15**, 3003–3011.
28 I. M. AlNashef, M. L. Leonard, M. C. Kittle, M. A. Matthews and J. W. Weidner, *Electrochem. Solid-State Lett.*, 2001, **4**, D16–D18.
29 I. M. AlNashef, M. L. Leonard, M. A. Matthews and J. W. Weidner, *Ind. Eng. Chem. Res.*, 2002, **41**, 4475–4478.
30 M. T. Carter, C. L. Hussey, S. K. Strubinger and R. A. Osteryoung, *Inorg. Chem.*, 1991, **30**, 1149–1151.
31 M. Hayyan, M. A. Hashim and I. M. AlNashef, *Chem. Rev.*, 2016, **116**, 3029–3085.
32 M. Hayyan, F. S. Mjalli, I. M. AlNashef and M. A. Hashim, *J. Fluorine Chem.*, 2012, **142**, 83–89.
33 M. Hayyan, F. S. Mjalli, M. A. Hashim and I. M. AlNashef, *Ind. Eng. Chem. Res.*, 2012, **51**, 10546–10556.
34 M. Hayyan, F. S. Mjalli, M. A. Hashim, I. M. AlNashef and X. M. Tan, *J. Electroanal. Chem.*, 2011, **657**, 150–157.
35 M. M. Islam, T. Imase, T. Okajima, M. Takahashi, Y. Niikura, N. Kawashima, Y. Nakamura and T. Ohsaka, *J. Phys. Chem. A*, 2009, **113**, 912–916.
36 K. U. Schwenke, J. Herranz, H. A. Gasteiger and M. Piana, *J. Electrochem. Soc.*, 2015, **162**, A905–A914.
37 M. Hayyan, A. M. Alakrach, A. Hayyan, M. A. Hashim and H. F. Hizaddin, *ACS Sustainable Chem. Eng.*, 2017, **5**, 1854–1863.
38 M. Hayyan, F. S. Mjalli, I. M. AlNashef and M. A. Hashim, *J. Fluorine Chem.*, 2012, **142**, 83–89.
39 I. M. AlNashef, M. A. Hashim, F. S. Mjalli, M. Q. A.-h. Ali and M. Hayyan, *Tetrahedron Lett.*, 2010, **51**, 1976–1978.
40 M. Hayyan, F. S. Mjalli, M. A. Hashim and I. M. AlNashef, *J. Mol. Liq.*, 2013, **181**, 44–50.
41 S. Doblinger, J. Lee and D. S. Silvester, *J. Phys. Chem.*, 2019, **123**, 10727–10737.
42 Y. Katayama, H. Onodera, M. Yamagata and T. Miura, *J. Electrochem. Soc.*, 2004, **151**, A59.
43 M. C. Buzzeo, O. V. Klymenko, J. D. Wadhawan, C. Hardacre, K. R. Seddon and R. G. Compton, *J. Phys. Chem. A*, 2003, **107**, 8872–8878.
44 J. Sun, M. Forsyth and D. R. Macfarlane, *J. Phys. Chem. B*, 1998, **102**, 8858–8864.
45 H. Ashassi-Sorkhabi, A. Kazempour and P. Salehi-Abar, *J. Mol. Liq.*, 2018, **251**, 190–200.
46 B. Wang, L. Qin, T. Mu, Z. Xue and G. Gao, *Chem. Rev.*, 2017, **117**, 7113–7131.
47 M. Hayyan, M. Ibrahim, A. Hayyan and M. A. Hashim, *Braz. J. Chem. Eng.*, 2017, **34**, 227–239.
48 M. Hayyan, M. H. Ibrahim, A. Hayyan, I. M. AlNashef, A. M. Alakrach and M. A. Hashim, *Ind. Eng. Chem. Res.*, 2015, **54**, 12263–12269.
49 M. Hornig and A. Klamt, *J. Chem. Inf. Model.*, 2005, **45**, 1169–1177.
50 C. Steffen, K. Thomas, U. Huniar, A. Hellweg, O. Rubner and A. Schroer, *J. Comput. Chem.*, 2010, **31**, 2967–2970.
51 J. P. Perdew, *Phys. Rev. B: Solid State*, 1986, **33**, 8822.
52 A. Schäfer, C. Huber and R. Ahlrichs, *J. Chem. Phys.*, 1994, **100**, 5829–5835.
53 M. J. Frisch, G. W. Trucks, H. B. Schlegel, G. E. Scuseria, M. A. Robb, J. R. Cheeseman, G. Scalmani, V. Barone, G. A. Petersson, H. Nakatsuji, X. Li, M. Caricato, A. V. Marenich, J. Bloino, B. G. Janesko, R. Gomperts, B. Mennucci, H. P. Hratchian, J. V. Ortiz, A. F. Izmaylov, J. L. Sonnenberg, F. WilliamsDing, F. Lipparini, F. Egidi, J. Goings, B. Peng, A. Petrone, T. Henderson, D. Ranasinghe, V. G. Zakrzewski, J. Gao, N. Rega, G. Zheng, W. Liang, M. Hada, M. Ehara, K. Toyota, R. Fukuda, J. Hasegawa, M. Ishida, T. Nakajima, Y. Honda, O. Kitao, H. Nakai, T. Vreven, K. Throssell, J. A. Montgomery, Jr., J. E. Peralta, F. Ogliaro, M. J. Bearpark, J. J. Heyd, E. N. Brothers, K. N. Kudin, V. N. Staroverov, T. A. Keith, R. Kobayashi, J. Normand, K. Raghavachari, A. P. Rendell, J. C. Burant, S. S. Iyengar, J. Tomasi, M. Cossi, J. M. Millam, M. Klene, C. Adamo, R. Cammi, J. W. Ochterski, R. L. Martin, K. Morokuma, O. Farkas, J. B. Foresman and D. J. Fox, *Gaussian 09*, Gaussian Inc., Wallingford CT, 2009.
54 P. K. Chattaraj, U. Sarkar and D. R. Roy, *Chem. Rev.*, 2006, **106**, 2065–2091.

55 P. K. Chattaraj and S. Giri, *Annu. Rep. Prog. Chem., Sect. C: Phys. Chem.*, 2009, **105**, 13–39.
56 A. Klamt, F. Eckert and W. Arlt, *Annu. Rev. Chem. Biomol. Eng.*, 2010, **1**, 101–122.
57 F. Eckert and A. Klamt, COSMOtherm, Version C2. 1, Release 01. 11, COSMOlogic, GmbH & Co. KG, Leverkusen, Germany, 2010.
58 C. D. Sessler, M. Rahm, S. Becker, J. M. Goldberg, F. Wang and S. J. Lippard, *J. Am. Chem. Soc.*, 2017, **139**, 9325–9332.
59 D.-W. Yoon, D. E. Gross, V. M. Lynch, J. L. Sessler, B. P. Hay and C.-H. Lee, *Angew. Chem.*, 2008, **47**, 5038–5042.
60 N. Galamba, A. Paiva, S. Barreiros and P. Simões, *J. Chem. Theory Comput.*, 2019, **15**, 6277–6293.
61 S. J. Pike, J. J. Hutchinson and C. A. Hunter, *J. Am. Chem. Soc.*, 2017, **139**, 6700–6706.
62 J. Schwöbel, R.-U. Ebert, R. Kühne and G. Schüürmann, *J. Chem. Inf. Model.*, 2009, **49**, 956–962.
63 J. J. Dannenberg, *Chem. Rev.*, 1999, **99**, 1225–1242.
64 G. D. Purvis, 3rd, *J. Comput.-Aided Mol. Des.*, 1991, **5**, 55–80.
65 J. Weber, P. Fluekiger, P. Y. Morgantini, O. Schaad, A. Goursot and C. Daul, *J. Comput.-Aided Mol. Des.*, 1988, **2**, 235–253.
66 K. Fukui, *Science*, 1982, **218**, 747–754.
67 F. De Proft, N. Sablon, D. J. Tozer and P. Geerlings, *Faraday Discuss.*, 2007, **135**, 151–159.
68 J. S. Griffith and L. E. Orgel, *Q. Rev., Chem. Soc.*, 1957, **11**, 381–393.
69 R. M. Fogarty, R. P. Matthews, C. R. Ashworth, A. Brandt-Talbot, R. G. Palgrave, R. A. Bourne, T. V. Hoogerstraete, P. A. Hunt and K. R. J. Lovelock, *J. Chem. Phys.*, 2018, **148**, 193817.
70 R. S. Nicholson, *Anal. Chem.*, 1965, **37**, 1351–1355.
71 A. J. Bard, L. R. Faulkner, J. Leddy and C. G. Zoski, *Electrochemical methods: fundamentals and applications*, Wiley, New York, 1980.
72 J. Wang, *Analytical electrochemistry*, John Wiley & Sons, 2006.
73 O. U. Ahmed, F. S. Mjalli, T. Al-Wahaibi, Y. Al-Wahaibi and I. M. AlNashef, *Ind. Eng. Chem. Res.*, 2015, **54**, 2074–2080.
74 M. Hayyan, F. S. Mjalli, I. M. AlNashef and M. A. Hashim, *Int. J. Electrochem. Sci.*, 2012, **7**, 8116–8127.
75 J. L. Roberts, T. S. Calderwood and D. T. Sawyer, *J. Am. Chem. Soc.*, 1984, **106**, 4667–4670.
76 B.-A. Mei, O. Munteshari, J. Lau, B. Dunn and L. Pilon, *J. Phys. Chem. C*, 2018, **122**, 194–206.
77 M. E. Orazem and B. Tribollet, *Electrochemical Impedance Spectroscopy*, John Wiley & Sons, 2011.
78 V. Lates, A. Falch, A. Jordaan, R. Peach and R. J. Kriek, *Electrochim. Acta*, 2014, **128**, 75–84.
79 R. M. Torresi, L. Lodovico, T. M. Benedetti, M. R. Alcântara, C. Debiemme-Chouvy and C. Deslouis, *Electrochim. Acta*, 2013, **93**, 32–43.
80 T. Jänsch, J. Wallauer and B. Roling, *J. Phys. Chem. C*, 2015, **119**, 4620–4626.
81 T. Kai, M. Zhou, S. Johnson, H. S. Ahn and A. J. Bard, *J. Am. Chem. Soc.*, 2018, **140**, 16178–16183.

